

Article

Copper-Containing Mixed Metal Oxides (Al, Fe, Mn) for Application in Three-Way Catalysis

Tim Van Everbroeck ¹, Radu-George Ciocarlan ¹, Wouter Van Hoey ¹, Myrjam Mertens ²
and Pegie Cool ^{1,*}

¹ Laboratory of Adsorption and Catalysis, Department of Chemistry, University of Antwerp, Universiteitsplein 1, 2610 Wilrijk, Belgium; Tim.Vaneverbroeck@uantwerpen.be (T.V.E.); Radu-George.Ciocarlan@uantwerpen.be (R.-G.C.); Wouter.VanHoey@uantwerpen.be (W.V.H.)

² VITO Flemish Institute for Technological Research, Boeretang 200, B-2400 Mol, Belgium; myrjam.mertens@vito.be

* Correspondence: Pegie.Cool@uantwerpen.be

Received: 8 October 2020; Accepted: 17 November 2020; Published: 19 November 2020



Abstract: Mixed oxides were synthesized by co-precipitation of a Cu source in combination with Al, Fe or Mn corresponding salts as precursors. The materials were calcined at 600 and 1000 °C in order to crystallize the phases and to mimic the reaction conditions of the catalytic application. At 600 °C a mixed spinel structure was only formed for the combination of Cu and Mn, while at 1000 °C all the materials showed mixed spinel formation. The catalysts were applied in three-way catalysis using a reactor with a gas mixture containing CO, NO and O₂. All the materials calcined at 600 °C displayed the remarkable ability to oxidize CO with O₂ but also to reduce NO with CO, while the pure oxides such as CuO and MnO₂ were not able to. The high catalytic activity at 600 °C was attributed to small supported CuO particles present and imperfections in the spinel structure. Calcination at 1000 °C crystallized the structure further which led to a dramatic loss in catalytic activity, although CuAl₂O₄ and CuFe₂O₄ still converted some NO. The materials were characterized by X-ray diffraction (XRD), Raman spectroscopy, H₂-Temperature Programmed Reduction (H₂-TPR), N₂-sorption and scanning electron microscopy with energy dispersive X-ray spectroscopy (SEM-EDX).

Keywords: spinel; copper oxide; three-way catalysis; NO reduction; CO oxidation

1. Introduction

Even with the most recent advances in alternatively-powered vehicles 86.8% of all the new-car registrations in the EU were fueled by diesel or petrol. The largest share of these accounted to the petrol cars (57.3% of the EU market) [1]. So even though most research nowadays is focused on technology for alternatively-powered vehicles, there is still a lot of fundamental research necessary to cope with the ever-increasing demand in petrol cars. Petrol cars are using three-way catalytic converters to abate the release of CO, volatile organic compounds (VOCs) (hydrocarbons) and NO_x to the environment. This technology uses critical raw materials (CRMs) such as Pt, Pd and Rh as the main catalytic materials [2,3]. The reason why these materials are considered critical is related to their great economic importance, while their supply is at risk. This means that the existing technologies need to be adapted in order to reduce the amount of CRMs. One way to reduce the use of CRMs is to replace them with alternative catalytic materials.

A comparison between the specific reaction rates for the oxidation of CO shows that the most interesting materials to replace Pd are Co₃O₄ (having a reaction rate 20 times lower) or CuO (having 50 times lower reaction rate) [4]. Since cobalt is also considered a CRM [3], the logical choice is to study CuO. To compensate for the low specific reaction rate (e.g., mL CO₂/(min. m²), larger amounts of CuO

(tens of percent) than are regularly used of the precious materials (<1%) can be used. Moreover, the amount of available catalytic surface area can be increased by using porous support materials. Other ways of increasing the reaction rate consider the generation of synergies between different materials by using mixtures of oxides [5,6]. By treatment at high temperatures, these mixtures can grow into new crystal structures of mixed oxides such as spinels and perovskites [7]. Another important factor in defining a valuable catalyst is related with the stability in order to be reused in several catalytic cycles. Here, in particular, it is important to investigate if these mixed oxides are also effective for real-world applications, as the materials will have to endure long exposures to high temperatures and many cycles of work.

In this work, we chose to investigate mixtures of CuO with aluminum-, iron- and manganese oxides. All of these elements are abundant and therefore ideal to be used as a catalyst in large productions. The other aspect they all have in common is that they commonly occur in a trivalent state in oxides (Al_2O_3 , Fe_2O_3 , Mn_2O_3). However, they differ in the existence of other stable oxidation states of the metals. The difference is that Al^{3+} cannot be reduced to Al^{2+} , Fe^{3+} is reducible to Fe^{2+} , and Mn^{3+} can be reduced to Mn^{2+} and oxidized to Mn^{4+} . This is important with respect to their role in the catalytic conversion mechanism.

The mixture of copper and manganese oxides is quite known for the oxidation of CO under the name “hopcalite”. Originally, this was developed during the first World War to remove CO from air in gasmasks [5,8,9]. One of the most active forms of the mixture consists of 60% MnO_2 and 40% CuO [5,9]. Most literature that feature hopcalite-like mixtures focus on oxidation reactions only such as CO [6,10–13] or VOCs [14–16] and not on the simultaneous removal of NO as in the case of three-way catalysis.

Al, Fe and Mn oxides can co-exist in the same structure with CuO and form different spinel-type structures. The formation of these types of mixed oxides enhances the dispersion factor of elements, when compared with composite materials (separate oxide forms). In order for this to happen, most of the times a specific ratio (1:2) of the elements must be applied and thermal treatments must be used. The classical spinel structure follows the general formula $\text{A}^{2+}\text{B}^{3+}_2\text{O}_4$, which can also be noted as the two types of oxides (A^{2+}O)($\text{B}^{3+}_2\text{O}_3$). The A and B represent the two sites of the spinel structure, namely tetrahedral—A and octahedral—B, respectively. With regards to the cation sites occupancy, one can define three different types of spinel structures: (I) Normal spinel—in which the divalent cation (A^{2+}) is fully occupying the tetrahedral site, (II) inverse spinel—where the divalent (A^{2+}) cation is totally occupying the octahedral site, while half of the trivalent (B^{3+}) is occupying the tetrahedral site and (III) spinel structures with a different inversion degree—where the divalent (A^{2+}) and trivalent (B^{3+}) are occupying both sites of the structure [17]. In other words, a more general formula for spinels would be $(\text{A}_{(1-x)}\text{B}_x)^{\text{tet}}[\text{A}_x\text{B}_{(2-x)}]^{\text{oct}}\text{O}_4$ with x being the inversion parameter. This means that if x is 0, the spinel is normal, while if x is 1 it is inverse [18]. Cu and Mn are quite peculiar elements to be incorporated in the spinel structure because they display the Jahn–Teller effect [19]. This means that the octahedral Cu^{2+} , Mn^{2+} and Mn^{3+} [20] are tetragonally distorted. While these distortions make both elements more difficult to incorporate in a mixed oxide, this seems to be compensated when they are used together in copper manganite [21]. CuFe_2O_4 occurs mostly as an inverse spinel with only about 6–24% Cu in the A sites [22–24]. For CuMn_2O_4 reports vary between 25 and 80% inversion [25–27]. In bulk CuAl_2O_4 x is around 0.4 which means about 60% of Cu is in the tetrahedral sites [18,28,29].

In this research work, we synthesized mixtures of oxides by co-precipitation of Cu-salts with Al, Fe or Mn salts. A 1:2 ratio between Cu and the other element was used to encourage the formation of a spinel form. In the case of Mn, also 1:1 ratio was used to see if there was an influence on the catalytic performance. These materials were calcined at 600 and 1000 °C which are representing the temperatures of the catalytic converter in normal and extreme conditions. In order to keep the testing conditions simple, the materials were tested as powders in a flow of CO, NO and O_2 instead of a full mixture for three-way catalysts consisting of CO, H_2 , different hydrocarbons, O_2 , CO_2 , H_2O and NO. This way it is easier to evaluate the ability of the materials to oxidize CO and to reduce NO. The materials

were characterized by X-ray diffraction (XRD), Raman spectroscopy, H₂-Temperature Programmed Reduction (H₂-TPR), N₂-sorption and Scanning Electron Microscopy with Energy Dispersive X-ray Spectroscopy (SEM-EDX).

2. Results

2.1. Physicochemical Properties of the Catalysts

Figure 1 displays the X-ray diffractograms (XRD) of CuAl 600 and CuAl 1000. After the calcination at 600 °C, the aluminum is not detected as a crystal structure of Al₂O₃ or CuAl₂O₄, suggesting the formation of amorphous alumina or small particles of CuAl₂O₄. On the other hand, Cu is clearly present as CuO (tenorite), in a monoclinic crystal arrangement. The detailed crystallites size data are presented in Table 1. The approximate size of the CuO crystallites, calcined at 600 °C and calculated from the (111) reflection at 38.7°, is 10 nm. Noticeably, after the calcination at 1000 °C, the Bragg reflections of CuAl₂O₄ appear, suggesting the formation of a well-defined spinel structure at this elevated temperature when compared to 600 °C. The CuO average crystallites size is around 44 nm, while the CuAl₂O₄ average crystallites size is roughly 56 nm, taking into account the (113) reflection at 36.9° for the latter component. SEM-EDX (Supplementary Table S1) proved that in both cases the Cu-Al ratio is the same; about 36 wt% Al and 64 wt% Cu, which means a molar ratio of about 1.3:1 Al:Cu instead of 2:1. This leads to the conclusion that the sample contains more Cu and explains the presence of large CuO crystallites.

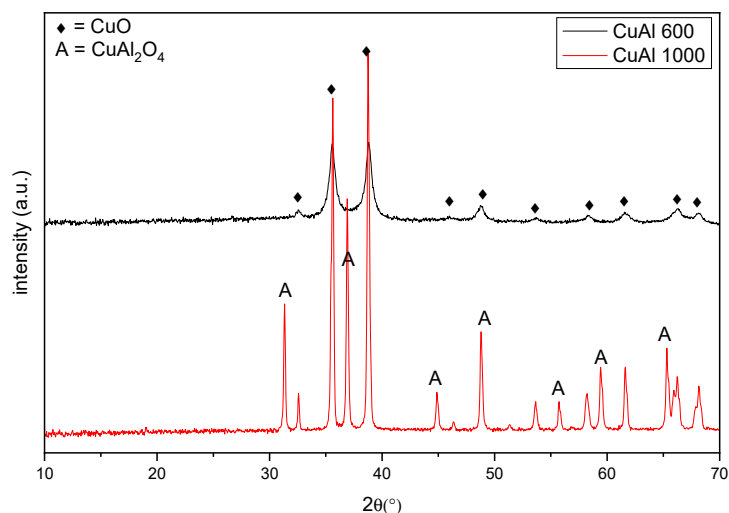


Figure 1. XRD of CuAl calcined at 600 and 1000 °C.

Table 1. Estimated average crystallite size based on XRD.

Catalyst/Size (nm)	CuO	Spinel
CuAl 600	10	-
CuFe 600	17	-
CuMn 600	11	22
CuMn2 600	-	33
CuAl 1000	44	56
CuFe 1000	46	62
CuMn 1000	26	63
CuMn2 1000	-	56

The XRD patterns of the CuFe samples are shown in Figure 2. Here, after the thermal treatment at 600 °C, a mixture of oxides is observed, with hematite (Fe₂O₃), magnetite (Fe₃O₄) and tenorite (CuO) phases present. On the other hand, at 1000 °C only the spinel structure of CuFe₂O₄ and tenorite (CuO)

are observed. CuO phase shows an increase of the crystallites size from 17 nm to 46 nm when calcined at 600 °C and 1000 °C, respectively (Table 1).

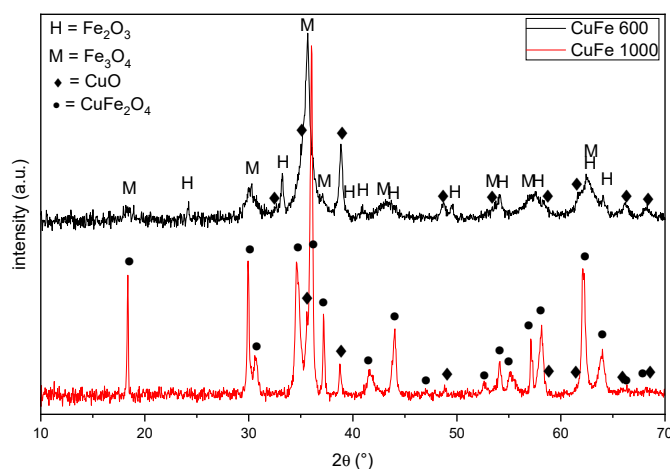


Figure 2. XRD of CuFe calcined at 600 and 1000 °C.

Figure 3 shows the diffractograms of different Cu-Mn samples (Cu:Mn = 1:1 = CuMn, Cu:Mn = 1:2 = CuMn2). In both cases, at 600 °C the crystal structure of $\text{Cu}_{1.5}\text{Mn}_{1.5}\text{O}_4$ is present in the composites. This structure has been reported in previous studies in literature [10,14,19,30,31]. After the calcination at 1000 °C, the structure is slightly changed in both ratios of the Cu:Mn systems. A clear evidence of this modification is observed for the reflections at 57.6° and 63.3°, which represent the (115) and (044) plane, respectively (Figure 4). For CuMn 1000, an extra tenorite (CuO) phase, with a size of 26 nm, is detected in the XRD. In the case of CuMn2, where more Mn is present than necessary to form $\text{Cu}_{1.5}\text{Mn}_{1.5}\text{O}_4$, a segregated bixbyite phase (Mn_2O_3) is obtained from the additional Mn. At 1000 °C, the Mn phase formed is hausmannite, which is written as $\text{Mn}^{2+}\text{Mn}_2^{3+}\text{O}_4^{2-}$, and its crystal structure arrangement is similar to a tetragonally deformed spinel [32].

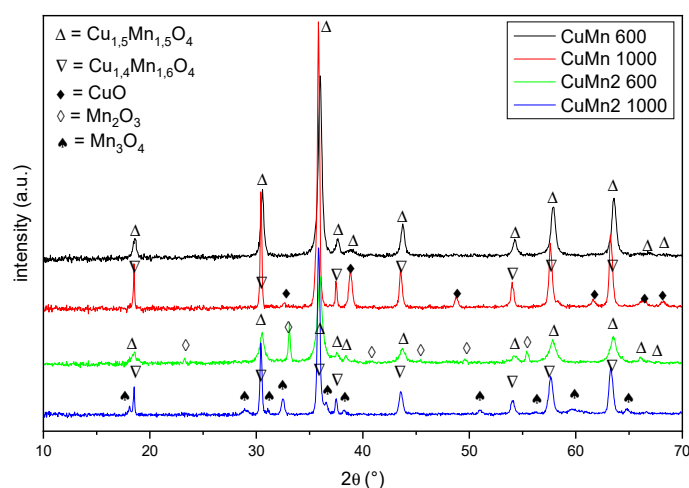


Figure 3. XRD of CuMn and CuMn2 calcined at 600 and 1000 °C.

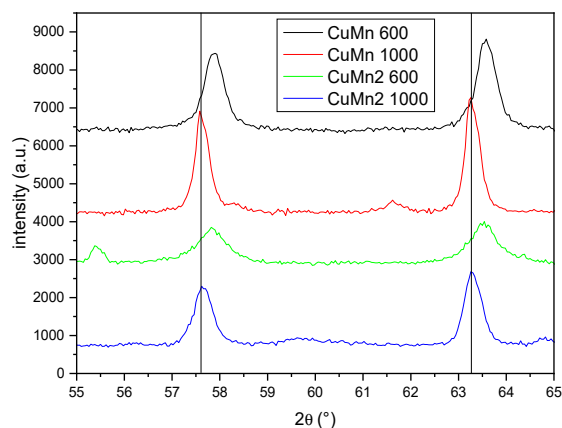


Figure 4. Detail of the XRD of CuMn and CuMn2 calcined at 600 and 1000 °C.

Raman spectroscopy is used to identify the phases that are not distinguished from XRD analysis. The spectra that are presented here are obtained by focusing on areas where CuO is less present, so that the spectra would mostly display the other phases.

Figure 5 shows the Raman spectra of CuAl 600 and CuAl 1000. From the microscopy images, grey areas with black spots were visible. For this reason, the beam was focused on the light colored areas, where the typical signals of CuO are very low. For CuO, only three optical phonon modes ($A_g + 2 B_g$) out of nine ($4A_u + 5B_u + A_g + 2B_g$) are Raman active. These are found at 288 cm^{-1} (A_g), 330 and 621 cm^{-1} (B_g), with a weak intensity in the presented spectra [33]. The remaining bands match very well with those predicted for $\gamma\text{-Al}_2\text{O}_3$ by Liu et al. [34]. In the mentioned study, the phonon frequencies were calculated for a spinel (as $\gamma\text{-Al}_2\text{O}_3$ is usually described as a defective spinel) and a non-spinel model, based on the dehydration of boehmite $\gamma\text{-Al}_2\text{O}_3$. There are 57 Raman active modes for the spinel model: 34 A_g and 23 B_g , while for the non-spinel mode there are 60 (34 A_g and 26 B_g). The peaks in the spectra at 210 , 370 , 410 , 490 , 560 , 640 and 670 cm^{-1} match well with the most intense peaks observed in the theoretical study for the spinel model, while the relative intensity and Raman shift of the peaks at 740 and 810 cm^{-1} match rather with those of the non-spinel model.

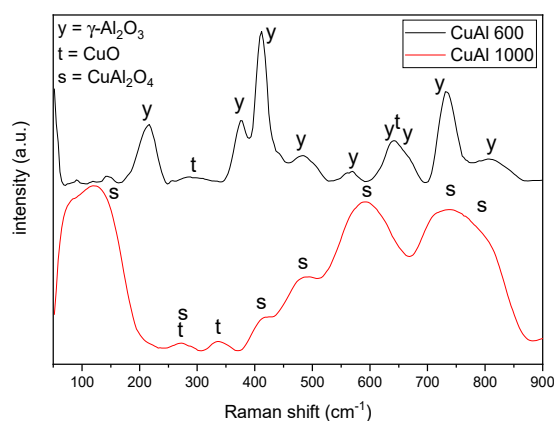


Figure 5. Raman spectra of CuAl 600 and CuAl 1000.

On the other hand, the Raman spectrum of CuAl 1000 is completely different from that of CuAl 600. Again, the signals of CuO are not very intense at 288 and 330 cm^{-1} . All the other bands represent the contribution of CuAl_2O_4 . According to literature, only five modes can be observed ($A_{1g} + E_g + 3F_{2g}$). The band at 790 cm^{-1} can be assigned to A_{1g} , at 270 , 590 , 710 cm^{-1} to F_{2g} and 475 cm^{-1} to E_g [35–37].

For CuFe 600, the Raman modes (Figure 6) are clearly assignable to hematite (Fe_2O_3). This material is characterized by seven Raman active modes, (I) two A_{1g} modes are found at 220 and 490 cm^{-1} ,

(II) three of the five E_g modes are found at 290, 400 and 600 cm^{-1} , while (III) the remaining two are very weak in intensity and are normally found at 250 and 300 cm^{-1} [38].

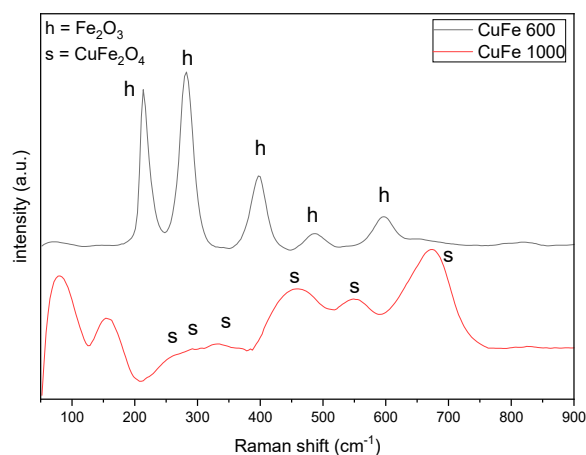


Figure 6. Raman spectra of CuFe 600 and CuFe 1000.

The bands of CuFe 1000 are very broad which makes it difficult to distinguish between the separate structures' modes. The typical bands of the cubic copper ferrite structure can still be distinguished. There are five Raman active modes ($A_{1g} + E_g + 3F_{2g}$) for cubic copper ferrite. Bands at 220, 460 and 560 cm^{-1} can be assigned to F_{2g} modes, while the band at 280 and 660 cm^{-1} can be assigned to the E_g and A_{1g} band [39,40]. Another band can be found between 300 and 400 cm^{-1} .

Finally, in Figure 7 the Raman spectra of the manganese containing compounds are presented. Similar to the previous spinel compound, five Raman active modes ($A_{1g} + E_g + 3F_{2g}$) are expected to appear. The band at 650 cm^{-1} can again be assigned to A_{1g} and at 430 cm^{-1} to E_g . Around 350, 470 and 580 cm^{-1} the F_{2g} modes are found [41]. The Raman active optical modes of Mn_2O_3 (bixbyite) are found at 309, 500 and 640 cm^{-1} which is close to those of CuO (280, 330 and 621 cm^{-1}) [42]. For this reason, only the mode at 500 cm^{-1} is definite evidence for the presence of Mn_2O_3 . The Raman active modes of Mn_3O_4 (hausmannite) (310, 365, 472, 650 cm^{-1}) are in this case also difficult to distinguish from those of the copper manganite spinel structure as this material also has the spinel structure and most of the bands overlap.

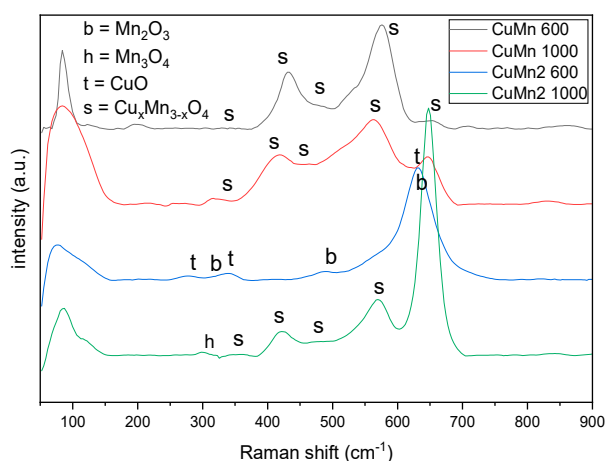


Figure 7. Raman spectra of CuMn 600, CuMn 1000, CuMn2 600 and CuMn2 1000.

H_2 -TPR provides information about the reducibility of the catalysts and the technique is used to compare the different samples. The reduction profiles are represented as a function of temperature (Figure 8). The profile of bulk CuO is added as a reference material. For CuO, the onset of reduction

appears around 275 °C with the maximum being at 330 °C. The peaks for the as-prepared materials are in all the cases very broad, which makes it difficult to conclude any statements on speciation. One noticeable observation about these results is that all the materials calcined at 600 °C have their onset temperatures at significantly lower temperatures than bulk CuO, which means that the CuO particles are very small and in a dispersed state in the samples or have become more reducible, due to interactions with the other metal oxide [6,13,43–45]. The lowest onset temperature can be found for CuMn 600 although all the synthesized materials show a peak under 250 °C, probably due to highly dispersed CuO present on the other oxide but not bound to it. Both CuMn 600 and CuMn2 600 already show reduction above 350 °C due to Cu²⁺ in the spinel phase. After the calcination at 1000 °C, the difference between the materials becomes larger with the onset temperature being under 350 °C for CuFe 1000 and CuAl 1000 while it's closer to 400 °C for CuMn2 1000. In this case, the difference is probably due to the fact that CuO is reduced easier than Cu in the spinel structure. In all the cases, there is a more than 100 °C shift between the calcination at 600 °C and 1000 °C, proving that Cu²⁺ in the spinel structure is less reducible when the crystallinity is increased for this mixed oxide structure.

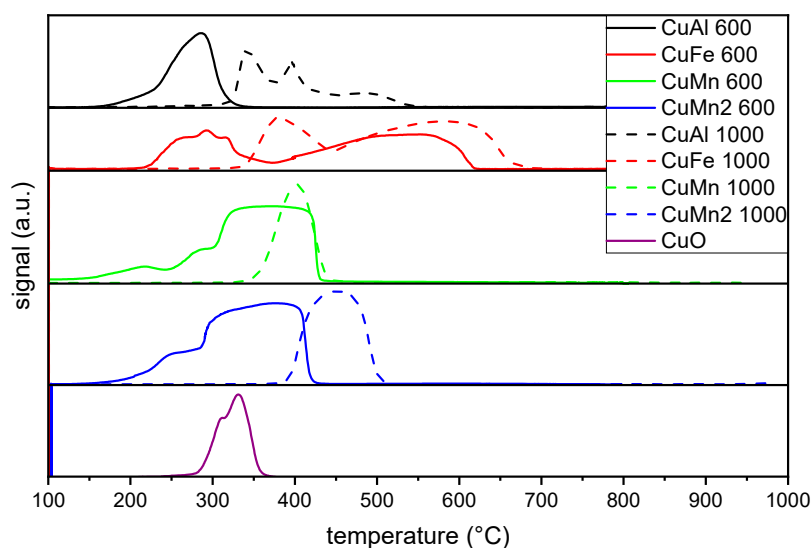


Figure 8. H₂-TPR of the synthesized materials and CuO.

2.2. Catalytic Activity

In this research work, the catalytic performance test is done with an O₂ content much lower than stoichiometrically necessary to oxidize all the CO. In this way, the O₂ conversion is used to compare the ability of the catalysts to oxidize CO with O₂ (Reaction 1), while at the same time, the NO conversion is used to compare the ability to reduce NO with CO (Reaction 2). Figures 9–11 present the CO, NO and O₂ conversion for each of the catalysts calcined at 600 °C on the left and calcined at 1000 °C on the right side. Figure 12 shows the conversions for the pure oxides CuO and MnO₂, while Table 2 presents the light-off temperatures (onset temperature of significant catalytic activity) [46]. In case of O₂, we take the temperature at which 50% is converted (T₅₀ O₂), which is typically used, and for NO the temperature at which 20% NO is converted (T₂₀ NO), as 50% is almost never achieved in the current experiments. Moreover, Table 2 depicts the reaction rates for CO at 200 °C and for NO at 550 °C, in terms of mol of the reactant converted per second, for a gram of catalyst. As most of the catalytic reactions take place at the surface of a catalyst, one must take into account the corresponding surface area, in order to accurately assess the performance. For this reason, Table 2 also lists the BET specific surface area and specific reaction rate at 200 °C for CO and at 550 °C for NO. The specific reaction rate describes the converted amount of reactant per second per m² of catalyst surface area. The supporting information includes the graphs of the specific reaction rates (Supplementary Figures S9 and S10), as a function of temperature, in the regions where it is not limited by the reactants. Due to the low surface

area of the catalysts calcined at 1000 °C (even under 1 m²/g), the calculated rates are incredibly large and extremely sensitive to experimental errors, compared to the materials calcined at 600 °C. Taking this into account, it is very likely that the performance per m² of the materials calcined at 1000 °C is overestimated, leading to the conclusion that it is possible more layers of the material than just the surface are involved in the reaction. For this reason, the calculated turnover frequencies based on the total mol of Cu present in each sample (Table 2) provide a better view of the results. The corresponding graphs are also presented in the supporting information (Supplementary Figures S11 and S12).

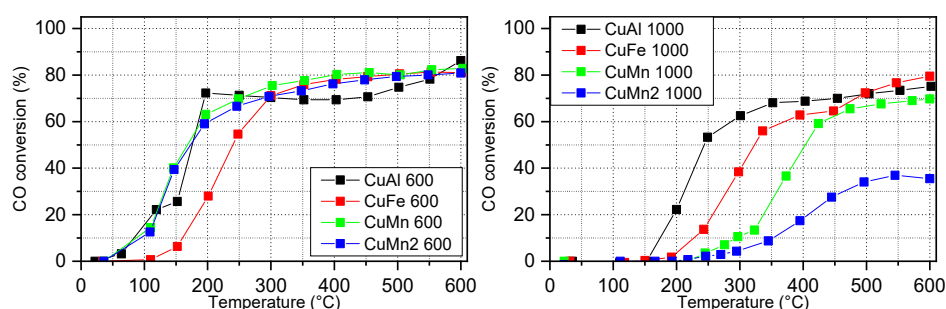


Figure 9. CO conversion of the materials calcined at 600 °C (left) and 1000 °C (right).

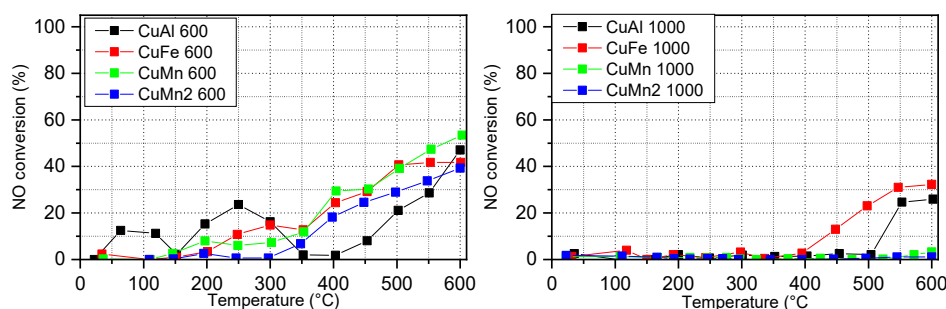


Figure 10. NO conversion of the materials calcined at 600 °C (left) and 1000 °C (right).

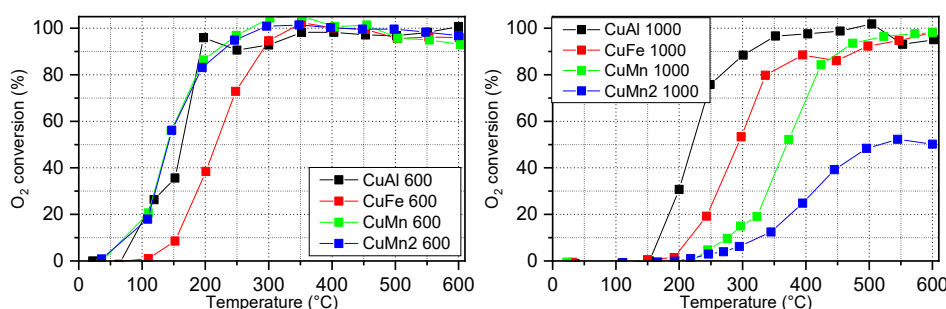


Figure 11. O₂ conversion of the materials calcined at 600 °C (left) and 1000 °C (right).

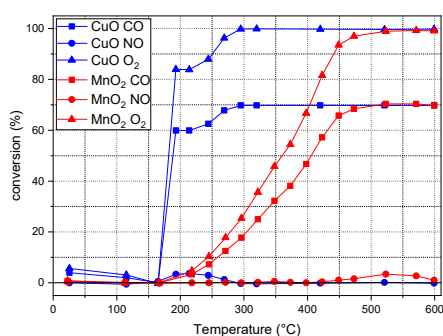


Figure 12. CO, NO and O₂ conversion for CuO and MnO₂.

Table 2. Temperatures of 50% O₂ (T₅₀ O₂) conversion and 20% NO conversion (T₂₀ NO), BET specific surface area (SSA), seaction rates (RR), specific reaction rates (SRR) and turnover frequencies (TOF).

-	T ₅₀ O ₂	T ₂₀ NO	SSA	RR _{CO}	Spec. RR _{CO}	TOF _{CO}	RR _{NO}	Spec. RR _{NO}	TOF _{NO}
-	-	-	-	at 200 °C	at 200 °C	at 200 °C	at 550 °C	at 550 °C	at 550 °C
-	(°C)	(°C)	(m ² /g)	(mol. s ⁻¹ . g _{cat} ⁻¹)	(mol. s ⁻¹ (m ²) ⁻¹)	(h ⁻¹)	(mol. s ⁻¹ . g _{cat} ⁻¹)	(mol. s ⁻¹ (m ²) ⁻¹)	(h ⁻¹)
CuAl 600	178	390	129	1.56 × 10 ⁻⁶	1.21 × 10 ⁻⁸	1.21	1.97 × 10 ⁻⁶	1.53 × 10 ⁻⁶	0.152
CuFe 600	217	384	49	5.71 × 10 ⁻⁷	1.17 × 10 ⁻⁸	0.82	2.88 × 10 ⁻⁶	5.90 × 10 ⁻⁶	0.413
CuMn 600	140	377	36	1.32 × 10 ⁻⁶	3.61 × 10 ⁻⁸	1.12	3.23 × 10 ⁻⁶	8.86 × 10 ⁻⁶	0.276
CuMn2 600	141	412	47	1.24 × 10 ⁻⁶	2.63 × 10 ⁻⁸	1.76	2.35 × 10 ⁻⁶	4.98 × 10 ⁻⁶	0.334
CuAl 1000	221	543	3	4.60 × 10 ⁻⁷	1.32 × 10 ⁻⁷	0.36	1.61 × 10 ⁻⁶	4.63 × 10 ⁻⁶	0.125
CuFe 1000	293	483	1	7.44 × 10 ⁻⁸	1.11 × 10 ⁻⁷	0.11	2.15 × 10 ⁻⁶	3.21 × 10 ⁻⁶	0.308
CuMn 1000	370	-	0.2	0	0	0.00	8.35 × 10 ⁻⁶	4.72 × 10 ⁻⁶	0.007
CuMn2 1000	516	-	0.1	4.20 × 10 ⁻⁹	3.02 × 10 ⁻⁸	0.01	7.85 × 10 ⁻⁶	5.64 × 10 ⁻⁶	0.011
CuO	182	-	1	1.55 × 10 ⁻⁶	1.69 × 10 ⁻⁶	0.44	0	0	0.000
MnO2	360	-	4	4.41 × 10 ⁻⁸	1.06 × 10 ⁻⁸	0.01	2.09 × 10 ⁻⁶	5.04 × 10 ⁻⁶	0.007

From these results it can be seen that pure CuO is already able to oxidize CO with O₂ at rather low temperatures (T₅₀ O₂ = 182 °C). Also MnO₂, supposedly the most active manganese oxide for CO oxidation [47,48], manages to do this although at a much higher temperature (T₅₀ O₂ = 360 °C). None of these simple oxides is however able to reduce NO in this catalytic test. The as-prepared materials calcined at 600 °C show an excellent catalytic performance able to convert CO with O₂ at even lower temperatures than CuO, with the exception of CuFe 600 (T₅₀ O₂ = 217 °C). Moreover, all these as-prepared materials are able to convert also NO, in contrast to the reference oxides CuO and MnO₂. It is surprising that the performance of NO conversion is very much alike in all cases. The CuAl 600 catalyst stands out, due to the appearance of two volcano plots at low temperatures, under 350 °C. This takes place because N₂O is selectively formed through Reaction 3 instead of Reaction 2 [49,50]. Furthermore, CuAl 600 has a much higher surface area than the other catalysts, which can result in to an advantage over the other materials. To compensate for this effect, one can compare the specific reaction rates for each catalyst. The values (Table 2) show that the performance of CuAl 600 for CO oxidation is rather comparable with that of CuFe 600 instead of CuMn 600 and CuMn2 600. At the same time, its NO performance is lower than the other samples at the higher temperature region. This is even more clear from the TOF_{NO}.



The materials calcined at 1000 °C display much more variations in their catalytic performances. In all the cases, the O₂ conversion takes place at higher temperatures than the reference material CuO. CuAl 1000 shows the lowest T₅₀ O₂, followed by CuFe 1000, CuMn 1000 and CuMn2 1000. After calcination at 1000 °C NO conversion is not detected for CuMn 1000 and CuMn2 1000. On the contrary, CuAl 1000 and CuFe 1000 still manage to convert 26 and 32% at 600 °C, which is still higher than the yield achieved for pure CuO. Moreover, all the materials have their surface area reduced by more than 97% after the calcination at 1000 °C, which brings it to a comparable level with the pure CuO sample. As an exception, only CuAl 1000 manages to keep a surface area above 1 m²/g, compared to all other samples calcined at 1000 °C.

3. Discussion

The characterization study of the catalysts shows that after the calcination at 600 °C, only the manganese containing materials featured crystals of a copper containing spinel structure. In the case of CuAl 600, the Raman study confirmed that this sample contains γ-Al₂O₃, which is also described as having a defective spinel structure. Certain bands in the Raman spectrum imply not only the formation of a spinel type alumina, but also of non-spinel type alumina. The calcination at 1000 °C is forcing copper into the alumina structure, forming a CuAl₂O₄ spinel structure. A large amount of copper remains outside of this structure in the form of CuO (as SEM-EDX pointed out), since the amount of aluminum is lower than stoichiometrically required to form spinel. Part of the Al is washed away during the washing step, in the form of the soluble Al(OH)₄⁻, which is the dominant species at high pH [51]. This is the reason why the synthesis method is adapted in this case, so that the pH is kept as low as possible, while still being able to precipitate the Cu species. However, as the results show, part of the Al is inevitably washed away.

In CuFe 600 the CuFe₂O₄ structure is not crystallized but magnetite (Fe₃O₄), having an inverse spinel structure, is present [52]. Just like in the case of alumina, the magnetite will incorporate copper in its structure at higher temperatures, to form CuFe₂O₄. Because Fe₃O₄ and CuFe₂O₄ are very alike in structure, it is possible that CuFe 1000 still contains some Fe₃O₄, which explains the extra CuO phase.

In the Cu-Mn materials the spinel-like phase matches with the structure that is reported as $\text{Cu}_{1.5}\text{Mn}_{1.5}\text{O}_4$ instead of CuMn_2O_4 . This structure has a simple cubic system (P 4₁ 3 2), but after calcination at 1000 °C the structure shifts towards the familiar face-centered cubic spinel structure (Fd $\bar{3}$ m). Many literature reports state that pure CuMn_2O_4 samples could not be prepared [19,21,30,53]. Rapid quenching from sinter temperature results in a tetragonal structure, while slowly cooling, as is the case here, leads to cubic spinel phases contaminated with extra phases [19,21]. CuMn 1000 shows an increase in the size of CuO which could also be evidence that the copper manganite is eliminating copper to transform from $\text{Cu}_{1.5}\text{Mn}_{1.5}\text{O}_4$ towards CuMn_2O_4 .

It is not surprising that at 600 °C highly crystalline phases of spinel are not present, as often very high temperatures (above 1000 °C) with very long sintering times (e.g., 48 h) are used [19,54,55]. In this study, the calcination temperatures are chosen to pursue the conditions of the automotive catalyst, under normal conditions, between 400 and 600 °C and about 900 °C for high power operations, which are normally only met briefly [4].

The Raman spectra of CuAl 1000, CuFe 1000 and CuMn 1000 (Figures 5–7) confirm the formation of spinel structures with the apparition of broad bands in the specific regions. The broadening pattern of the bands could possibly be due to defects in the structure, which leads to deviations from the perfectly cubic structure. Another reason for the broad bands' formation can be correlated with the modification of the inversion degree in the spinel structure. This fact is strictly depending on the preference of the cations to occupy one of the two sites, with regards to the synthesis method and calcination temperature. As a result, if the Cu^{2+} and Fe^{3+} cations are occupying both the tetrahedral sites, the Raman mode around 700 cm^{-1} characteristic to A_{1g} symmetry of the tetrahedral site is split in two different energy bands, due to the different atomic masses of the cations [56]. Bands broadening in Raman spectroscopy of solids is often associated with the materials being amorphous or containing very small crystals [57]. However, here it is not the case, since one would expect a higher crystallinity after the thermal treatment at 1000 °C compared to 600 °C.

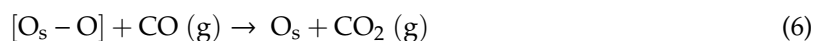
In the spectra of CuFe 1000 (Figure 6), most of the bands are attributed to the cubic copper ferrite structure, while other do not match this structure. Chatterjee et al. report the appearance of some extra bands at 388 cm^{-1} together with a weak band at 625 cm^{-1} , which is likely also the case here. In their study, the reason for the extra bands is related to the exciting radiation of the Raman laser (532 nm), being larger than the particle diameter [40].

For all the materials, the presence of maxima under 200 cm^{-1} is still under debate. Lazarevic et al. suggest that translational movement of the whole tetrahedron is the reason of these modes [58]. Saravanakumar et al. support the idea of a Jahn–Teller effect of Cu(II) ions, which leads to a lowering lattice symmetry of F_{2g} mode [59]. Pekov et al. correlate the presence of the strong band at 125 cm^{-1} with the lattice modes [60].

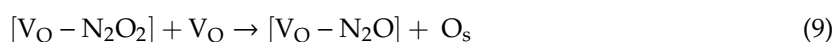
The catalytic tests prove that the composites calcined at 600 °C are indeed better for CO oxidation and NO reduction reactions than the separate oxides. After the calcination at 1000 °C, CuAl 1000 and CuFe 1000 are still showing NO conversion at higher temperature, while pure CuO does not, which is impressive for materials with such a low surface area. From the characterization of the materials calcined at 600 °C, one would expect a different performance for the manganese containing compounds in comparison to the others, as copper manganite is crystallized at much lower temperatures than the other spinels.

Both mechanism of CO oxidation and NO reduction are based on the Mars–Van Krevelen mechanism, which means the metal oxide surface has an active part in the reaction [45,61–63]. For the oxidation of CO, CO adsorbs first to the metal cation and abstracts an O from the surface (O_s), leaving behind an oxygen vacancy (V_o) as CO_2 desorbs. If O_2 is present, it will bind to the surface filling the vacancy with one O while the other O can bind to a new CO molecule to form CO_2 , which leaves the surface restored to its original state, so that the catalytic cycle can restart [63]. This mechanism is depicted below:





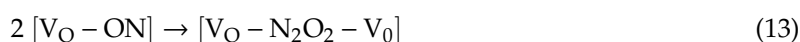
For NO reduction it is required that the oxygen vacancies are formed first by interaction with CO, as displayed in Reaction (4), so that NO can adsorb there with its oxygen. Different mechanisms are proposed for NO reduction on metal oxides, but always they involve the presence of two neighboring oxygen vacancies [62,64,65]. This means that there is a competition between O₂ and NO for the oxygen vacancies in tests like this, while the NO reduction is having the great disadvantage of needing two neighboring vacancies in order to take place. For brevity reasons, we are not showing all the possible mechanisms here or make any statements on which of the possible mechanisms (Eley–Rideal or Langmuir–Hinshelwood) take place in our studied systems, since this is not the purpose of the study. Below, an Eley–Rideal mechanism (Reaction 7–10) is presented. A first NO adsorbs to a first vacancy and a second NO reacts from the gas phase, forming an adsorbed N₂O₂. The oxygen of the second NO gets abstracted by the second vacancy leaving behind an adsorbed N₂O which decomposes to N₂ filling the first vacancy with oxygen.



In case there is no adjacent vacancy the adsorbed N₂O₂ can also lose oxygen to the surface and desorb as N₂O (Reaction 11). This can explain the N₂O formation at low temperature, as stated before.



In a possible Langmuir–Hinshelwood mechanism, the second NO adsorbs to the second vacancy and forms a bidentate N₂O₂ with the other adsorbed NO. N₂ is obtained, restoring the oxygen at the surface.



From the mechanisms it can be concluded that the most important factor for NO reduction is providing enough vacancies for NO to adsorb to. Patel et al. claim that CuAl₂O₄ is able to reduce NO better than CuO, due to the dissimilarly charged metal-oxygen configuration (Cu²⁺-O-Al³⁺), which makes the structure more susceptible for electron transfer [66]. The structure remains stable during the changing of the oxidation states and on top of that, bulk CuAl₂O₄ is more conductive than Al₂O₃, which makes it easier to share free electrons in the whole structure. In other words, the vacancies created by the reduction with CO can be better stabilized. This pathway is envisioned in Figure 13.

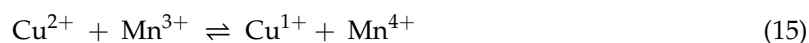


Figure 13. Reduction by CO on CuAl₂O₄.

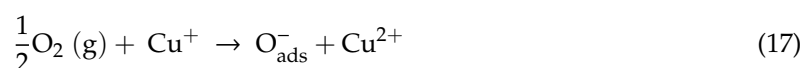
Although this reasoning explains the NO reduction at high temperatures for CuAl 1000 and CuFe 1000 as opposed to CuO where there is no activity at all, this does not explain the catalytic results of the materials calcined at 600 °C. XRD and Raman clearly show that CuAl 600 consists of CuO and γ-Al₂O₃ in clear contrast with the CuAl₂O₄ of CuAl 1000. It is very likely that some Cu diffuses into

the Al₂O₃ matrix in CuAl 600 forming “surface aluminate” as it is often reported [66–69]. However, in the work of Patel et al. [66,67] it is stated that as opposed to bulk aluminate, this surface aluminate is a lot less effective in NO reduction because the reduced copper ions do not have the conductive field around them as in bulk aluminate. They order the species from most effective to least effective for NO reduction as bulk CuAl₂O₄ > CuO > surface CuAl₂O₄. Our results show however that the enhanced performance for NO reduction and CO oxidation as well, is rather due to the effect of supporting smaller crystals of CuO on the other oxide than due to the formation of spinel. The low onset temperature in H₂-TPR is also characteristic for highly dispersed copper oxide and is certainly related to the high CO oxidation [43]. The estimated CuO crystallites size is also smaller for CuAl 600 than for CuFe 600, which correlates with the lower T₅₀ O₂ and H₂-TPR onset temperature. The extra CuO in CuMn 1000 compared to CuMn2 1000 also explains the better CO conversion. The energy cost for the generation of oxygen vacancies is much lower on steps and corners than on a perfect surface of a metal oxide, so smaller crystals will have a larger surface to bulk ratio and more low-coordinated ions at edges, which explains the lower reduction temperature [45,70]. The mixture of CuO and Fe₂O₃ in CuFe 600 did not show any improvement for CO oxidation compared to CuAl 600, which indicates there is probably also no spill-over effect of oxygen from Fe₂O₃ to CuO that improves the reducibility [6].

Now, a very interesting observation is that the copper-manganese materials formed a totally different system than the other materials. At 600 °C, they did not consist of crystals of the separate oxides, but mostly of the non-stoichiometric spinel Cu_{1.5}Mn_{1.5}O₄, while at 1000 °C the materials consist of a spinel together with an extra phase of CuO or Mn₃O₄. Thus, the catalytic behavior cannot be explained by the same reasoning as before. As mentioned in the introduction, Mn³⁺ can also be oxidized to Mn⁴⁺, and studies are showing that in copper manganese spinels a solid state charge transfer redox system exists that oxidizes Mn³⁺ to Mn⁴⁺ and reduces Cu²⁺ to Cu¹⁺ [71]. Accordingly, in this spinel system, the most stable configuration has Cu¹⁺ in the tetrahedral spots and Mn⁴⁺ in the octahedral.



In this way, the mechanism for CO oxidation is explained by the adsorption of CO on Mn⁴⁺ and the adsorption of O₂ onto Cu¹⁺ [6,72].



This mechanism is quite peculiar as it suggests the involvement of two sites, while the previous one (Reaction 4 to 6) is explained with only one site. This ability to exchange electrons between Cu and Mn can also be seen as a way to stabilize the vacancies for NO reduction, similar to the before mentioned theory (Figure 13).

The experiments of Spassova et al. show that CO interacts first with the oxygen of the catalysts surface and that NO only starts to reduce afterwards [73]. This means the mechanism is similar to the ones mentioned before (Reaction 4 to 14). The research of Spassova et al. also pointed out that in the presence of O₂, the mechanism for NO reduction can first go through the oxidation of NO to NO₂, as follows:



In this way, O₂ is prevented from re-oxidizing the surface, so that the catalytic cycle will not restart and none of the NO will be reduced, but instead NO₂ covers the surface and forms nitrites that can decompose through Reaction 20. On top of this, NO₂ is reduced faster with CO than NO [74].

The question arising is why the catalytic performance of the copper manganites is not very good here? These materials apparently perform best when they are still amorphous [6,72]. As shown also here, the materials have already formed spinel crystals by calcination at 600 °C, while this was not the case for copper aluminate and copper ferrite. Crystallization causes a great reduction in surface area and the concentration of surface-active centers. The spinel crystal structure formed at 600 °C is not perfect, which explains also why it still changed by the calcination at 1000 °C and its defects in the $\text{Cu}_{1.5}\text{Mn}_{1.5}\text{O}_4$ structure together with the remaining mixture of more amorphous or small CuO and Mn_2O_3 particles are actually responsible for the catalytic activity. The generally underwhelming performance of all the spinels calcined at 1000 °C is related to the lower amount of defects present in the structure, which are representing the sites where oxygen vacancies require less energy to be formed. The surface areas of all the materials has been reduced by more than 97% after calcination at 1000 °C. The tested mixed oxides represent a very good alternative for three-way catalysis after some small modifications. They will have to be loaded onto a supporting material with a high surface area, via a strong interaction in order to prevent the crystal structures from growing too much during the exposure to the real working conditions of three-way catalysis.

4. Materials and Methods

4.1. Chemicals

All chemicals were purchased from Sigma-Aldrich/Merck, Darmstadt, Germany and used without further purification. The used chemicals are: $\text{Cu}(\text{NO}_3)_2 \cdot 3\text{H}_2\text{O}$ (99.0%), $\text{Al}(\text{NO}_3)_3 \cdot 9\text{H}_2\text{O}$ (100%), $\text{Fe}(\text{NO}_3)_3 \cdot 9\text{H}_2\text{O}$ (99.0%), MnCl_2 (97.0%), sodium hydroxide (NaOH) (100%), CuO (100%), MnO_2 (100%).

4.2. Catalyst Preparation

Spinel type materials were prepared by a simple co-precipitation reaction between the corresponding metal nitrate salts, or chloride in the case of manganese, with NaOH. In a first step, the appropriate volume of $\text{Cu}(\text{NO}_3)_2 \cdot 3\text{H}_2\text{O}$ solution (0.2 M) is mixed with the required volume of Al/Fe/Mn-salt solution (0.2 M). This mixture is refluxed at 80 °C for 30 min and 3 M NaOH solution is added. The pH of the mixture is maintained around 14, in order to precipitate the metals. In case of $\text{Al}(\text{NO}_3)_3$ precipitation, the sodium hydroxide solution was added very carefully and slowly, until the metals were precipitated (pH~11). This was visually observed by the change of color, from light blue to black. Further, the mixture is stirred at 80 °C for 1 h. Finally, the precipitate was separated and washed thoroughly with water until neutral pH is reached and calcined at 600 or 1000 °C for 4 h. In the case of 600 °C thermal treatment, the ramping speed was 1 °C/min, while in the case of 1000 °C the ramping speed was 2 °C/min. For simplicity, the samples were denoted as follows, according to the ratio between the metals: Cu:Al = 1:2 = CuAl, Cu:Fe = 1:2 = CuFe, Cu:Mn = 1:1 = CuMn, Cu:Mn = 1:2 = CuMn2. The number after the code indicates the calcination temperature.

4.3. Physicochemical Characterisation

The structural analysis of the annealed samples was performed by powder X-ray Diffraction (XRD) using an X-ray diffractometer (PANalytical X'Pert PRO MPD) equipped with $\text{Cu}_{K\alpha}$ radiation ($\lambda = 0.15406$ nm); measurements were done in the 2θ range from 20° to 80° using a bracket sample holder with a scanning speed of 0.04°/4 s in continuous mode. The crystallite size distribution was approximated using the Scherrer equation:

$$d = \frac{K\lambda}{\beta \cos(\theta)} \quad (21)$$

where d = crystallite size, λ = the wavelength of the X-ray source (0.15406 nm), β = the full width at half maximum of the chosen diffraction peak (2θ), θ the Bragg angle and K = the shape constant chosen

as 0.9. Using this equation, morphological effects and disorder to reflection widths were not taken into account so the obtained values were merely used for relative comparison of the materials [75].

Raman spectra were obtained on a Micro-Raman Horiba (Xplora Plus Microscope) equipped with a 532 nm laser. The range was between 50–1000 cm^{-1} Raman shift. The instrument is equipped with a 100× magnification microscope objective.

Temperature programmed reduction measurements with hydrogen (H_2 -TPR) were performed on a Quantachrome iQ. About 20 mg of the sample was outgassed at 200 °C for 16h prior to the measurements and then weighed again after cooling. The sample was then pre-treated under a He flow for 1 h. Reduction was done with a 5% H_2/Ar flow a rate of 25 mL/min. The temperature was raised between 100 and 800 °C at 10 °C/min. The hydrogen consumption was monitored with a thermal conductivity detector (TCD). These signals were normalized by the outgassed catalyst weight.

SEM-EDX was used to determine the surface composition using a FEG-ESEM-EDX, FEI Quanta 250 by scanning the whole field instead of discrete points.

N_2 -physisorption measurements were carried out on a Quantachrome Quadrasorb SI automated gas adsorption system. Prior to the measurements, the samples were outgassed at 200 °C for 16 h. The specific surface area (SSA) was calculated using the Brunauer–Emmet–Teller (BET) equation.

4.4. Catalytic Activity Measurements

The catalytic performance was tested in a fixed bed continuous flow quartz reactor, with a total gas flow rate of 200 mL/min. The tested powders were pelletized using an IR pelletizer, crushed and sieved in order to obtain a particle size between 150 and 300 μm . 200 mg of the sieved powder was loaded in the reactor and pre-treated under the same gas flow as during the test. The speed ramping from room temperature to 600 °C was 10 °C/min, maintaining this temperature for 1 h and then cooling back to room temperature. The catalytic test was done by ramping with 10 °C/min from room temperature to 600 °C and holding the temperature about every 50 °C for at least 10 min, in order to have a constant conversion value of the measurement. Figure 14 illustrates the protocol in a relevant timescale. The levels of CO and NO, from which the conversions were calculated, were measured using a Dräger polytron 7000 CO-detector and a 7Solutions GDS-15JP1-CA-NO NO-detector, respectively. The experimental set-up is illustrated in Figure 15. The conversion of O_2 was calculated from the conversion of CO, assuming that all NO conversion was due to the reaction between CO and NO to form N_2 (Reaction 2). The following formula was used for the O_2 conversion:

$$X_{\text{O}_2} = \frac{\left[X_{\text{CO}} - X_{\text{NO}} \cdot \left(\frac{C_{\text{in,NO}}}{C_{\text{in,CO}}} \right) \right] C_{\text{in,CO}}}{2 C_{\text{in,O}_2}} \quad (22)$$

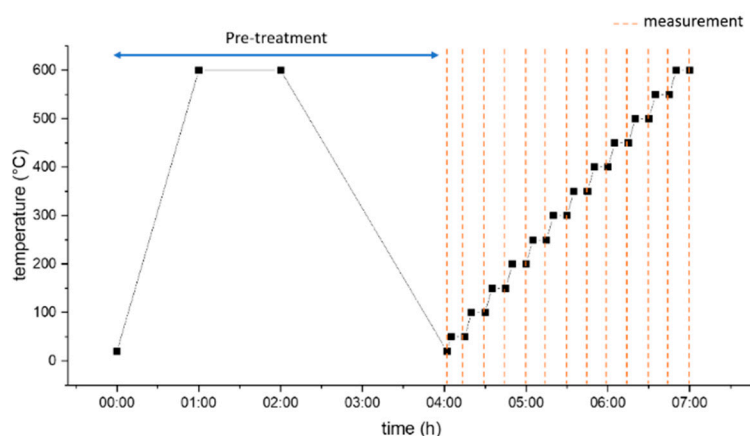


Figure 14. Temperature protocol of the catalytic test in a relevant timescale.

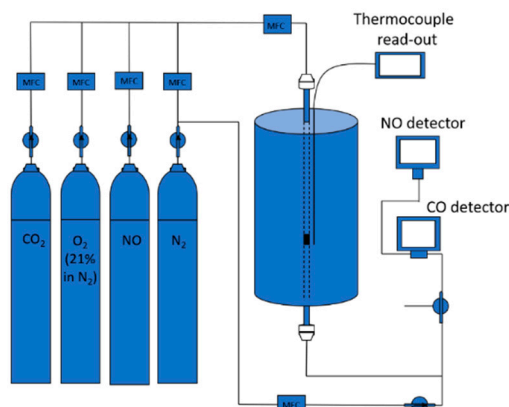


Figure 15. Experimental set-up for the catalytic tests.

With X being the conversion and C_{in} the input concentration.

The concentrations of the gases in the mixtures were as follows: CO: 3000 ppm, NO: 1000 ppm, O₂: 1050 ppm with N₂ being the balance gas.

The reaction rate (RR) of CO and NO was calculated as follows (example for CO):

$$RR_{CO} = \frac{C_{in,CO} \cdot X_{CO} \cdot F \cdot p}{T \cdot R \cdot g_{cat}} \quad (23)$$

F is the total flow rate, p the pressure (1.013 bar), T the temperature, R the gas constant. g_{cat} the weight of the catalyst.

The specific reaction rate (Spec. RR) is calculated as:

$$\text{Spec. RR} = \frac{RR}{SSA} \quad (24)$$

With SSA being the BET specific surface area.

The turnover frequency (TOF) is calculated as follows:

$$\text{TOF} = \frac{RR}{\# \text{ mol CuO} / g_{cat}} \quad (25)$$

The # mol CuO/ g_{cat} was calculated from the SEM-EDX results.

5. Conclusions

Mixed oxides were synthesized by co-precipitation of a Cu source in combination with Al, Fe or Mn corresponding salts as precursors. The materials were calcined at 600 and 1000 °C in order to crystallize the phases. Of the synthesized materials calcined at 600 °C only the manganese containing materials formed the crystal structure of a mixed spinel. The other materials consisted of mixtures of CuO with Al₂O₃ or iron oxides (Fe₂O₃ and Fe₃O₄). After the calcination at 1000 °C, all the materials featured a copper spinel structure, often accompanied by a separate CuO phase which shows that the formation of the spinel was not yet fully complete. Instead of the anticipated stoichiometric spinel CuMn₂O₄, a variant richer in copper, Cu_{1.5}Mn_{1.5}O₄, was formed both times at 600 °C. At 1000 °C the structure slightly changed probably towards a variant with less copper.

The as-synthesized materials show excellent performance in three-way catalysis. The prepared catalysts calcined at 600 °C could oxidize CO at lower temperatures than CuO, except for CuFe 600. All these materials were able to convert NO in these tests, while pure CuO was not able to do so. After calcination at 1000 °C, CO oxidation only occurred at higher temperatures. CuAl 1000 and CuFe 1000 still showed NO conversion although at higher temperatures. The improved CO oxidation and NO reduction were mainly due to highly dispersed CuO or small CuO particles supported on the other

oxide, while the spinel formation was useful for NO reduction. The underwhelming performance of the spinels can be attributed to the growth of the crystals, which reduces the amount of available sites and defects in the structure. The research proves that the mixed oxides tested here have great potential to be applied in three-way catalysis but that crystal growth will need to be prevented to ensure a long lifetime of the catalyst. Copper oxide—aluminum oxide combinations or copper oxide—iron oxide combinations are more promising than copper oxide—manganese oxide combinations, due to the formation of large crystals at lower temperatures for the latter one.

Supplementary Materials: The following are available online at <http://www.mdpi.com/2073-4344/10/11/1344/s1>, Supplementary Table S1: wt% and ratio of the second element X (Al, Fe, Mn) to Cu, as determined by SEM-EDX, Supplementary Figure S1: SEM-EDX spectrum for CuAl 600, Supplementary Figure S2: SEM-EDX spectrum for CuAl 1000, Supplementary Figure S3: SEM-EDX spectrum for CuFe 600, Supplementary Figure S4: SEM-EDX spectrum for CuFe 1000, Supplementary Figure S5: SEM-EDX spectrum for CuMn 600, Supplementary Figure S6: SEM-EDX spectrum for CuMn 1000, Supplementary Figure S7: SEM-EDX spectrum for CuMn2 600, Supplementary Figure S8: SEM-EDX spectrum for CuMn2 1000, Supplementary Figure S9: Specific reaction rates for CO, Supplementary Figure S10: Specific reaction rates for NO, Supplementary Figure S11: TOF for CO, Supplementary Figure S12: TOF for NO.

Author Contributions: Conceptualization, T.V.E. and R.-G.C.; methodology, T.V.E., R.-G.C.; formal analysis, T.V.E., W.V.H., M.M.; investigation, T.V.E., W.V.H.; resources, P.C.; data curation, T.V.E.; writing—original draft preparation, T.V.E.; writing—review and editing, R.-G.C., P.C.; visualization, T.V.E.; supervision, P.C.; project administration, P.C.; funding acquisition, P.C. All authors have read and agreed to the published version of the manuscript.

Funding: This research was funded by the European Union’s Horizon 2020 Project Partial-PGMs (H2020-NMP-686086) and the FWO-Flanders (project no. G038215N.)

Acknowledgments: The authors like to thank K. De Wael and G. Nuyts from the AXES research group, Department of Chemistry, UA, for performing the SEM-EDX measurements.

Conflicts of Interest: The authors declare no conflict of interest.

References

1. European Automobile Manufacturers Association. Fuel Types of New Cars: Petrol +11.9%, Diesel −3.7%, Electric +80.5% in Fourth Quarter of 2019. Available online: <https://www.acea.be/press-releases/article/fuel-types-of-new-cars-petrol-11.9-diesel-3.7-electric-81.3-in-fourth-quart> (accessed on 11 June 2020).
2. Kumar, K.; Kumar, N.; Singh, H. Comprehensive Review of Three way Catalytic Converter. *International J. Adv. Res. Innov. Ideas Educ.* **2017**, *3*, 1188–1196.
3. European Commission. *European Commission Report on Critical Raw Materials and the Circular Economy Part. 1/3*; European Commission: Brussels, Belgium, 2018.
4. Kummer, J.T. Catalysts for automobile emission control. *Prog. Energy Combust. Sci.* **1980**, *6*, 177–199. [[CrossRef](#)]
5. Almquist, J.A.; Bray, W.C. The catalytic oxidation of carbon monoxide. I. Efficiency of the catalysts, manganese dioxide, cupric oxide and mixtures of these oxides. *J. Am. Chem. Soc.* **1923**, *45*, 2305–2322. [[CrossRef](#)]
6. Buciuman, F.C.; Patcas, F.; Hahn, T. A spillover approach to oxidation catalysis over copper and manganese mixed oxides. *Chem. Eng. Process. Process Intensif.* **1999**, *38*, 563–569. [[CrossRef](#)]
7. Cousin, P.; Ross, R.A. Preparation of mixed oxides: A review. *Mater. Sci. Eng. A* **1990**, *130*, 119–125. [[CrossRef](#)]
8. Bliss, A. Arthur Becket Lamb February 25, 1880—May 15, 1952. *J. Am. Chem. Soc.* **1955**, *77*, 5773–5780. [[CrossRef](#)]
9. Lamb, A.B.; Bray, W.C.; Frazer, J.C.W. The Removal of Carbon Monoxide from Air. *J. Ind. Eng. Chem.* **1920**, *12*, 213–221. [[CrossRef](#)]
10. Biemelt, T.; Wegner, K.; Teichert, J.; Lohe, M.R.; Martin, J.; Grothe, J.; Kaskel, S. Hopcalite nanoparticle catalysts with high water vapour stability for catalytic oxidation of carbon monoxide. *Appl. Catal. B Environ.* **2016**, *184*, 208–215. [[CrossRef](#)]
11. Dey, S.; Dhal, G.C.; Mohan, D.; Prasad, R. Study of Hopcalite (CuMnOx) Catalysts Prepared Through A Novel Route for the Oxidation of Carbon Monoxide at Low Temperature. *Bull. Chem. React. Eng. Catal.* **2017**, *12*, 393. [[CrossRef](#)]
12. Puckhaber, L.S.; Cheung, H.; Cocke, D.L.; Clearfield, A. Reactivity of copper manganese oxides. *Solid State Ion.* **1989**, *32–33*, 206–213. [[CrossRef](#)]

13. Clarke, T.J.; Davies, T.E.; Kondrat, S.A.; Taylor, S.H. Mechanochemical synthesis of copper manganese oxide for the ambient temperature oxidation of carbon monoxide. *Appl. Catal. B Environ.* **2015**. [[CrossRef](#)]
14. Behar, S.; Gonzalez, P.; Agulhon, P.; Quignard, F.; Świerczyński, D. New synthesis of nanosized Cu-Mn spinels as efficient oxidation catalysts. *Catal. Today* **2012**, *189*, 35–41. [[CrossRef](#)]
15. Napruszewska, B.D.; Michalik, A.; Walczyk, A.; Duraczyńska, D.; Dula, R.; Rojek, W.; Lityńska-Dobrzyńska, L.; Bahranowski, K.; Serwicka, E.M. Composites of Laponite and Cu-Mn Hopcalite-Related Mixed Oxides Prepared from Inverse Microemulsions as Catalysts for Total Oxidation of Toluene. *Materials* **2018**, *11*, 1365. [[CrossRef](#)] [[PubMed](#)]
16. Clarke, T.J.; Kondrat, S.A.; Taylor, S.H. Total oxidation of naphthalene using copper manganese oxide catalysts. *Catal. Today* **2015**. [[CrossRef](#)]
17. Zhao, Q.; Yan, Z.; Chen, C.; Chen, J. Spinels: Controlled Preparation, Oxygen Reduction/Evolution Reaction Application, and Beyond. *Chem. Rev.* **2017**, *117*, 10121–10211. [[CrossRef](#)]
18. O'Neill, H.S.C.; James, M.; Dollase, W.A.; Redfern, S.A.T. Temperature dependence of the cation distribution in CuAl_2O_4 spinel. *Eur. J. Mineral.* **2005**, *17*, 581–586. [[CrossRef](#)]
19. Vandenberghe, R.E.; Robbrecht, G.G.; Brabers, V.A.M. On the stability of the cubic spinel structure in the system Cu Mn O. *Mater. Res. Bull.* **1973**, *8*, 571–579. [[CrossRef](#)]
20. Fridrichová, J.; Bacik, P.; Ertl, A.; Wildner, M.; Dekan, J.; Miglierini, M. Jahn-Teller distortion of Mn 3+ -occupied octahedra in red beryl from Utah indicated by optical spectroscopy. *J. Mol. Struct.* **2017**, *1152*. [[CrossRef](#)]
21. Robbrecht, G.G.; Henriët-Iserentant, C.M. On the Lattice Parameters and the Tetragonal Distortion of the Copper and Cadmium Manganite Systems. *Phys. Status Solidi* **1970**, *41*, K43–K46. [[CrossRef](#)]
22. Zuo, X.; Yang, A.; Vittoria, C.; Harris, V. Computational study of copper ferrite (CuFe_2O_4). *J. Appl. Phys.* **2006**, *99*, 08M909. [[CrossRef](#)]
23. Anandan, S.; Selvamani, T.; Prasad, G.G.; Asiri, M.A.; Wu, J.J. Magnetic and catalytic properties of inverse spinel CuFe_2O_4 nanoparticles. *J. Magn. Magn. Mater.* **2017**, *432*, 437–443. [[CrossRef](#)]
24. Ciocarlan, R.G.; Arčon, I.; Pui, A.; Mertens, M.; Tusar, N.N.; Seftel, E.M.; Cool, P. In-depth structural characterization and magnetic properties of quaternary ferrite systems $\text{Co}_{0.5}\text{Zn}_{0.25}\text{M}_{0.25}\text{Fe}_2\text{O}_4$ (M = Ni, Cu, Mn, Mg). *J. Alloys Compd.* **2020**. [[CrossRef](#)]
25. Shoemaker, D.P.; Li, J.; Seshadri, R. Unraveling Atomic Positions in an Oxide Spinel with Two Jahn-Teller Ions: Local Structure Investigation of CuMn_2O_4 . *J. Am. Chem. Soc.* **2009**, *131*, 11450–11457. [[CrossRef](#)] [[PubMed](#)]
26. Waskowska, A.; Gerward, L.; Olsen, J.; Steenstrup, S.; Talik, E. CuMn_2O_4 : Properties and the high-pressure induced Jahn-Teller phase transition. *J. Phys. Condens. Matter* **2001**, *13*, 2549. [[CrossRef](#)]
27. Radhakrishnan, N.K.; Biswas, A.B. A neutron diffraction study of the spinel oxide CuMn_2O_4 . *Phys. Status Solidi* **1977**, *44*, 45–49. [[CrossRef](#)]
28. Friedman, R.M.; Freeman, J.J.; Lytle, F.W. Characterization of CuAl_2O_3 catalysts. *J. Catal.* **1978**, *55*, 10–28. [[CrossRef](#)]
29. Strohmeier, B.R.; Levden, D.E.; Field, R.S.; Hercules, D.M. Surface spectroscopic characterization of $\text{Cu Al}_2\text{O}_3$ catalysts. *J. Catal.* **1985**. [[CrossRef](#)]
30. Blasse, G. Ferromagnetism and ferrimagnetism of oxygen spinels containing tetravalent manganese. *J. Phys. Chem. Solids* **1966**, *27*, 383–389. [[CrossRef](#)]
31. Vandenberghe, R.E.; Legrand, E.; Scheerlinck, D.; Brabers, V.A.M. Neutron diffraction study of the cation ordering in $\text{Cu}_{1.5}\text{Mn}_{1.5}\text{O}_4$ and $\text{CuMg}_{0.5}\text{Mn}_{1.5}\text{O}_4$. *Acta Crystallogr. Sect. B* **1976**, *32*, 2796–2798. [[CrossRef](#)]
32. Jarosch, D. Crystal structure refinement and reflectance measurements of hausmannite, Mn_3O_4 . *Mineral. Petrol.* **1987**, *37*, 15–23. [[CrossRef](#)]
33. Xu, J.F.; Ji, W.; Shen, Z.X.; Li, W.S.; Tang, S.H.; Ye, X.R.; Jia, D.Z.; Xin, X.Q. Raman spectra of CuO nanocrystals. *J. Raman Spectrosc.* **1999**, *30*, 413–415. [[CrossRef](#)]
34. Liu, Y.; Cheng, B.; Wang, K.-K.; Ling, G.-P.; Cai, J.; Song, C.-L.; Han, G.-R. Study of Raman spectra for $\gamma\text{-Al}_2\text{O}_3$ models by using first-principles method. *Solid State Commun.* **2014**, *178*, 16–22. [[CrossRef](#)]
35. D'Ippolito, V.; Andreozzi, G.B.; Bersani, D.; Lottici, P.P. Raman fingerprint of chromate, aluminate and ferrite spinels. *J. Raman Spectrosc.* **2015**, *46*, 1255–1264. [[CrossRef](#)]
36. Tomar, N.; Ghanti, E.; Bhagi, A.K.; Nagarajan, R. Studies on the hydrolysis of $\{\text{Cu}[\text{Al}(\text{OPri})_4]_2\}$, a single source precursor for CuAl_2O_4 spinel. *J. Non. Cryst. Solids* **2009**. [[CrossRef](#)]
37. Ghanti, E.; Nagarajan, R. Synthesis of $\text{CuAl}_2(\text{acac})_4(\text{OiPr})_4$, its hydrolysis and formation of bulk CuAl_2O_4 from the hydrolyzed gels; a case study of molecules to materials. *Dalton Trans.* **2010**, *39*, 6056–6061. [[CrossRef](#)]

38. de Faria, D.L.A.; Venâncio Silva, S.; de Oliveira, M.T. Raman microspectroscopy of some iron oxides and oxyhydroxides. *J. Raman Spectrosc.* **1997**, *28*, 873–878. [[CrossRef](#)]
39. Balaji, M.; Chithra Lekha, P.; Pathinettam Padiyan, D. Core-shell structure in copper ferrite-polyaniline nanocomposite: Confirmation by laser Raman spectra. *Vib. Spectrosc.* **2012**. [[CrossRef](#)]
40. Chatterjee, B.K.; Bhattacharjee, K.; Dey, A.; Ghosh, C.K.; Chattopadhyay, K.K. Influence of spherical assembly of copper ferrite nanoparticles on magnetic properties: Orientation of magnetic easy axis. *Dalton Trans.* **2014**, *43*, 7930–7944. [[CrossRef](#)]
41. Yang, X.; Tang, W.; Liu, Z.; Makita, Y.; Ooi, K. Synthesis of lithium-rich $\text{Li}_x\text{Mn}_2\text{O}_4$ spinels by lithiation and heat-treatment of defective spinels. *J. Mater. Chem.* **2002**, *12*, 489–495. [[CrossRef](#)]
42. Han, Y.-F.; Chen, F.; Zhong, Z.; Ramesh, K.; Chen, L.; Widjaja, E. Controlled Synthesis, Characterization, and Catalytic Properties of Mn_2O_3 and Mn_3O_4 Nanoparticles Supported on Mesoporous Silica SBA-15. *J. Phys. Chem. B* **2006**, *110*, 24450–24456. [[CrossRef](#)]
43. Van Der Grift, C.J.G.; Mulder, A.; Geus, J.W. Characterization of silica-supported copper catalysts by means of temperature-programmed reduction. *Appl. Catal.* **1990**, *60*, 181–192. [[CrossRef](#)]
44. Choukroun, D.; Daems, N.; Kenis, T.; Van Everbroeck, T.; Hereijgers, J.; Altantzis, T.; Bals, S.; Cool, P.; Breugelmans, T. Bifunctional Nickel–Nitrogen-Doped-Carbon-Supported Copper Electrocatalyst for CO_2 Reduction. *J. Phys. Chem. C* **2020**, *124*, 1369–1381. [[CrossRef](#)]
45. Ruiz Puigdollers, A.; Schlexer, P.; Tosoni, S.; Pacchioni, G. Increasing Oxide Reducibility: The Role of Metal/Oxide Interfaces in the Formation of Oxygen Vacancies. *ACS Catal.* **2017**, *7*, 6493–6513. [[CrossRef](#)]
46. Biasin, A.; Fabro, J.; Michelon, N.; Glisenti, A.; Canu, P. Investigation of thermal effects on heterogeneous exothermic reactions and their impact on kinetics studies. *Chem. Eng. J.* **2019**. [[CrossRef](#)]
47. Iablokov, V.; Frey, K.; Geszti, O.; Kruse, N. High Catalytic Activity in CO Oxidation over MnOx Nanocrystals. *Catal. Lett.* **2010**, *134*, 210–216. [[CrossRef](#)]
48. Patel, A.; Shukla, P.; Chen, J.; Rufford, T.E.; Rudolph, V.; Zhu, Z. Activity of mesoporous-MnOx (m-MnOx) and CuO/m-MnOx for catalytic reduction of NO with CO. *Catal. Today* **2013**, *212*, 38–44. [[CrossRef](#)]
49. Okamoto, Y.; Gotoh, H.; Hishida, K.; Aritani, H.; Tanaka, T.; Yoshida, S. Surface copper-TiO₂ interaction species for NO-CO reactions. *Appl. Surf. Sci.* **1997**, *121–122*, 509–512. [[CrossRef](#)]
50. Okamoto, Y.; Gotoh, H. Copper-zirconia catalysts for NO-CO reactions. *Catal. Today* **1997**, *36*, 71–79. [[CrossRef](#)]
51. Emamjomeh, M.M.; Sivakumar, M.; Varyani, A.S. Analysis and the understanding of fluoride removal mechanisms by an electrocoagulation/flotation (ECF) process. *Desalination* **2011**, *275*, 102–106. [[CrossRef](#)]
52. Graves, P.R.; Johnston, C.; Campaniello, J.J. Raman scattering in spinel structure ferrites. *Mater. Res. Bull.* **1988**, *23*, 1651–1660. [[CrossRef](#)]
53. Buhl, R. Manganites spinelles purs d'elements de transition preparations et structures cristallographiques. *J. Phys. Chem. Solids* **1969**, *30*, 805–812. [[CrossRef](#)]
54. Areán, C.O.; Viñuela, J.S.D. Structural study of copper-nickel aluminate ($\text{Cu}_x\text{Ni}_{1-x}\text{Al}_2\text{O}_4$) spinels. *J. Solid State Chem.* **1985**, *60*, 1–5. [[CrossRef](#)]
55. Severino, F.; Brito, J.L.; Laine, J.; Fierro, J.L.G.; Agudo, A.L. Nature of Copper Active Sites in the Carbon Monoxide Oxidation on CuAl_2O_4 and CuCr_2O_4 Spinel Type Catalysts. *J. Catal.* **1998**, *177*, 82–95. [[CrossRef](#)]
56. da Silva, S.W.; Nakagomi, F.; Silva, M.S.; Franco, A.; Garg, V.K.; Oliveira, A.C.; Morais, P.C. Effect of the Zn content in the structural and magnetic properties of $\text{Zn}_x\text{Mg}_{1-x}\text{Fe}_2\text{O}_4$ mixed ferrites monitored by Raman and Mössbauer spectroscopies. *J. Appl. Phys.* **2010**, *107*, 09B503. [[CrossRef](#)]
57. Vandenberg, P. *Practical Raman Spectroscopy: An Introduction; Analytical Techniques in the Sciences*; Wiley: Hoboken, NJ, USA, 2013; ISBN 9781119961901.
58. Lazarević, Z.; Jovalekić, Ć.; Milutinović, A.; Sekulić, D.; Ivanovski, V.; Recnik, A.; Cekic, B.; Romčević, N. Nanodimensional spinel NiFe_2O_4 and ZnFe_2O_4 ferrites prepared by soft mechanochemical synthesis. *J. Appl. Phys.* **2013**, *113*. [[CrossRef](#)]
59. Saravanakumar, B.; Muthu Lakshmi, S.; Ravi, G.; Ganesh, V.; Sakunthala, A.; Yuvakkumar, R. Electrochemical properties of rice-like copper manganese oxide (CuMn_2O_4) nanoparticles for pseudocapacitor applications. *J. Alloys Compd.* **2017**, *723*, 115–122. [[CrossRef](#)]
60. Pekov, I.; Sandalov, F.; Koshlyakova, N.; Vigasina, M.; Polekhovskiy, Y.; Britvin, S.; Sidorov, E.; Turchkova, A. Copper in Natural Oxide Spinel: The New Mineral Thermaerogenite CuAl_2O_4 , Cuprospinel and Cu-Enriched Varieties of Other Spinel-Group Members from Fumaroles of the Tolbachik Volcano, Kamchatka, Russia. *Minerals* **2018**, *8*, 498. [[CrossRef](#)]

61. Mars, P.; van Krevelen, D.W. Oxidations carried out by means of vanadium oxide catalysts. *Chem. Eng. Sci.* **1954**, *3*, 41–59. [[CrossRef](#)]
62. Carlotto, S.; Natile, M.M.; Glisenti, A.; Vittadini, A. Catalytic Mechanisms of NO Reduction in a CO-NO Atmosphere at Co- and Cu-Doped SrTiO₃(100) Surfaces. *J. Phys. Chem. C* **2018**, *122*, 449–454. [[CrossRef](#)]
63. Carlotto, S.; Natile, M.M.; Glisenti, A.; Paul, J.-F.; Blanck, D.; Vittadini, A. Energetics of CO oxidation on lanthanide-free perovskite systems: The case of Co-doped SrTiO₃. *Phys. Chem. Chem. Phys.* **2016**, *18*, 33282–33286. [[CrossRef](#)]
64. Xie, S.; Rosynek, M.P.; Lunsford, J.H. Catalytic Reactions of NO over 0–7 mol% Ba/MgO Catalysts: I. The Direct Decomposition of NO. *J. Catal.* **1999**, *188*, 24–31. [[CrossRef](#)]
65. Vannice, M.A.; Walters, A.B.; Zhang, X. The Kinetics of NO_x Decomposition and NO Reduction by CH₄ over La₂O₃ and Sr/La₂O₃. *J. Catal.* **1996**, *159*, 119–126. [[CrossRef](#)]
66. Patel, A.; Shukla, P.; Chen, J.; Rufford, T.E.; Wang, S.; Rudolph, V.; Zhu, Z. Structural sensitivity of mesoporous alumina for copper catalyst loading used for NO reduction in presence of CO. *Chem. Eng. Res. Des.* **2015**, *101*, 27–43. [[CrossRef](#)]
67. Patel, A.; Shukla, P.; Pan, G.T.; Chong, S.; Rudolph, V.; Zhu, Z. Influence of copper loading on mesoporous alumina for catalytic NO reduction in the presence of CO. *J. Environ. Chem. Eng.* **2017**, *5*, 2350–2361. [[CrossRef](#)]
68. Zhu, Z.H.; Zhu, H.Y.; Wang, S.B.; Lu, G.Q. Preparation and Characterization of Copper Catalysts Supported on Mesoporous Al₂O₃ Nanofibers for N₂O Reduction to N₂. *Catal. Lett.* **2003**, *91*, 73–81. [[CrossRef](#)]
69. Shimizu, K.; Maeshima, H.; Satsuma, A.; Hattori, T. Transition metal-aluminate catalysts for NO reduction by C₃H₆. *Appl. Catal. B Environ.* **1998**, *18*, 163–170. [[CrossRef](#)]
70. Pinto, F.M.; Suzuki, V.Y.; Silva, R.C.; La Porta, F.A. Oxygen Defects and Surface Chemistry of Reducible Oxides. *Front. Mater.* **2019**, *6*, 260. [[CrossRef](#)]
71. Cocke, D.L.; Vepřek, S. First direct evidence of a solid state charge transfer redox system $\text{Cu}^{2+} + \text{Mn}^{3+} \rightleftharpoons \text{Cu}^{1+} + \text{Mn}^{4+}$ in copper manganese oxide. *Solid State Commun.* **1986**, *57*, 745–748. [[CrossRef](#)]
72. Vepřek, S.; Cocke, D.L.; Kehl, S.; Oswald, H.R. Mechanism of the deactivation of Hopcalite catalysts studied by XPS, ISS, and other techniques. *J. Catal.* **1986**, *100*, 250–263. [[CrossRef](#)]
73. Spassova, I.; Khristova, M.; Panayotov, D.; Mehandjiev, D. Coprecipitated CuO-MnO_x Catalysts for Low-Temperature CO-NO and CO-NO-O₂ Reactions. *J. Catal.* **1999**, *185*, 43–57. [[CrossRef](#)]
74. Gassan-zade, G.Z.; Mukherjee, T.K.; Alkhozov, T.G. Effect of oxygen on the catalytic reduction of nitric oxides by carbon monoxide over NiO. *React. Kinet. Catal. Lett.* **1979**, *12*, 525–529. [[CrossRef](#)]
75. Hargreaves, J.S.J. Some considerations related to the use of the Scherrer equation in powder X-ray diffraction as applied to heterogeneous catalysts. *Catal. Struct. React.* **2016**, *2*, 33–37. [[CrossRef](#)]

Publisher's Note: MDPI stays neutral with regard to jurisdictional claims in published maps and institutional affiliations.



© 2020 by the authors. Licensee MDPI, Basel, Switzerland. This article is an open access article distributed under the terms and conditions of the Creative Commons Attribution (CC BY) license (<http://creativecommons.org/licenses/by/4.0/>).